FISEVIER

Contents lists available at ScienceDirect

Acta Materialia

journal homepage: www.elsevier.com/locate/actamat



Full length article

Mechanical properties and microstructure evolution of Ti₂AlC under compression in 25–1100 °C temperature range



R. Benitez^{a,f}, W.H. Kan^{b,c}, H. Gao^a, M. O'Neal^a, G. Proust^d, A. Srivastava^e, M. Radovic^{e,*}

- ^a Department of Mechanical Engineering, Texas A&M University, College Station, TX 77843, USA
- ^b Australian Centre for Microscopy and Microanalysis, The University of Sydney, NSW 2006, Australia
- ^c School of Aerospace, Mechanical and Mechatronic Engineering, The University of Sydney, Sydney, NSW 2006, Australia
- ^d School of Civil Engineering, The University of Sydney, Sydney, NSW 2006, Australia
- ^e Department of Material Science and Engineering, Texas A&M University, College Station, TX 77843, USA
- f Department of Mechanical Engineering, University of Texas Rio Grande Valley, Edinburg, Texas 78539, USA

ARTICLE INFO

Article History: Received 28 September 2019 Revised 20 February 2020 Accepted 23 February 2020 Available online 27 February 2020

Keywords: MAX phases Hall-Petch effect Creep Grain refinement Grain boundary sliding

ABSTRACT

This study investigates the effects of the initial grain size and temperature (ranging from room temperature to $1100~^{\circ}\text{C}$) on the mechanical properties and microstructure evolution of Ti₂AlC MAX phase. A Hall-Petch like relationship is observed between compressive strength and the grain size below brittle-to-plastic transition temperature (BPTT). However, the compressive strength of fine-grained MAX phase decreases more rapidly with increasing temperature resulting in inverse Hall-Petch effect above BPTT. Results from postmortem EBSD analysis reveal complex microstructural evolution in both fine- and coarse-grained microstructures during loading at different temperatures. The pronounced drop in compressive strength for fine-grained microstructures at temperatures close to BPTT is attributed to creep induced grain boundary sliding resulting in texture development with more grains oriented for easy slip. In coarse-grained microstructures, no significant texture development is observed even though grain refinement occurs at all temperatures. A mathematical model has also been formulated to predict the experimentally observed grain size and temperature dependent variation in the compressive strength of Ti₂AlC over a wide range of grain sizes and test temperatures. The mathematical model accounts for the competing effects of Hall-Petch strengthening and high temperature creep induced softening mechanisms.

© 2020 Acta Materialia Inc. Published by Elsevier Ltd. All rights reserved.

1. Introduction

Ti₂AlC belongs to a family of ternary carbides and nitrides, referred to as MAX phases, that all share a common chemical formula $M_{n+1}AX_n$ (where M is early transition metal, A is mostly group 13 and 14 element, X is C or N, and N=1,2 or 3), nano-laminated hexagonal structure (space group P63/mmc) and a unique combination of metallic- and ceramic- like properties [1,2]. Like ceramics, most of them have high stiffness, low density, and low thermal expansion, but like metals, they are good thermal and electronic conductors, and most importantly, they are damage tolerant, thermal shock resistant and can be easily machined at room temperature with conventional carbide tooling [3–5].

Mechanically, polycrystalline MAX phases can be hardly classified as typical metals or ceramics since they show pseudo-ductile behavior in constrained deformation modes, in highly oriented microstructures, and at high temperatures while in unconstrained deformation,

E-mail address: mradovic@tamu.edu (M. Radovic).

especially in tension and at lower temperatures, they behave more like a typical brittle ceramic [3,5-7]. Since the late 90 s, their pseudoductile mechanical behavior has been attributed to basal plane dislocations and the way they form, move, assemble and annihilate. Transmission Electron Microscopy (TEM) studies showed that dislocations in MAX phases are numerous, but constrained to basal and only basal planes having Burgers vector of $b = \frac{1}{3}11\overline{2}0$ [8–10]. Basal plane dislocations arrange themselves either in dislocation walls (DW), e.g., as lowangle (LAGB) or high-angle grain boundaries (HAGB), normal to the basal planes, or in arrays parallel to the basal planes or dislocation pile ups (DP) [9,10]. The fact that dislocations in MAX phases are numerous, but constrained only to basal planes, renders them highly plastically anisotropic. Therefore, large internal and incompatibility stress states rapidly develop in polycrystalline MAX phases under applied stress, as grains favorably oriented for easy slip (soft grains) deform easily under applied load, which in turn rapidly transfers the load to hard grains, i.e., those not favorably oriented for slip [11-15]. However, what makes MAX phases different from other brittle materials with limited number of slip systems is that they can deform additionally by kinking and formation of kink bands (KB). The latter consist of

^{*} Corresponding author.

pair of DW of opposite signs [6,16–18] with the slight change of crystal orientation between them. It has been postulated most recently, that ripplocations, rather than dislocations, are responsible for the formation of KB commonly observed in deformed MAX phases [19–22]. Nevertheless, thanks to kinking, polycrystalline MAX phases do not fail rapidly due to buildup of incompatibility stresses and formation of Zener-Stroh type cracks [23–25] in grain boundaries, like other brittle materials with limited number of slip system. They fail rather gracefully in a pseudo-ductile manner, especially coarse-grained ones in which KBs form more easily and at lower stresses [6].

Another implication of the plastic anisotropy of MAX phases is their room temperature hysteretic stress-strain behavior which is quite unusual for elastically stiff materials. It is well documented by now that when MAX phases are subjected to cyclic loading-unloading at room temperature, either in tension or compression, their stressstrain response is non-linear elastic and hysteretic, with all but the first stress-strain hysteresis loops being closed, reversible and reproducible [7,14,15,18,26-28]. At lower stresses, their hysteretic behavior can be attributed to easy yielding of soft grains upon loading and buildup of elastic lattice strains in hard grains that are sufficient to drive reverse plastic flow of soft grains upon unloading, giving rise to very small permanent or plastic strain in first loading-unloading cycle, and hysteresis loops in any subsequent loading cycle [11,12,14,15]. At higher stresses, numerous DWs, and KBs form during first loading cycle, even in grains with hard orientation, leading to some cyclic hardening and much larger energy dissipation per loading cycle most likely as a result of movement (bowing) of dislocations in DWs, or KBs and incipient kink bands (IKBs) [14,15].

At higher temperatures, all MAX phases tested to date show a strain-rate dependent brittle-to-plastic transition, usually at a temperature between 800 - 1100 °C [6]. Above their brittle-to-plastic transition temperatures (BPTT), they can be deformed to strains exceeding 25%, in both tension and compression, and their stressstrain response becomes highly strain rate dependent [7]. This, together with the fact that all MAX phases tested to date exhibit well established secondary creep regime with constant creep rate, suggests that their mechanical response above BPTT can be explained as controlled by the competition between the rate at which internal stresses accumulate and the rate at which they relax [29-32]. In other words, when loaded fast essentially brittle failure occurs at very low strains even above BPTT; however when loaded slowly they creep and can deform to large strains before failure [30]. In general, the origin of internal (incompatibility) stresses can be traced back to their plastic anisotropy and formation of DPs, DWs and KBs [14,15]. The accumulation of DWs and KBs also leads to cyclic hardening with increasing number of loading cycles, phenomenon that was observed above BPTT in cyclic loading-unloading to the same amplitude stress [18,33]. However, the nature of the relaxation of internal stresses is still subject of debate at this point. Based on the fact that the fracture toughness of MAX phases drops above BPTT, unlike in typical materials exhibiting brittle-to-plastic transition due to activation of additional slip systems, it has been hypothesized that those stresses have to be relaxed by temperature-dependent grain boundary decohesion and/or delamination [6,18,34,35]. This conclusion was further supported by the fact that a significant fraction of large strains observed during loading above BPTT can be attributed to the accumulated damages [7,31]. Most recently, Guitton et al. [36], showed evidence of cross-slip in prismatic and pyramidal planes in post mortem TEM studies of Ti₂AlN loaded at 900 °C, and proposed that the increase of available glide systems at high temperature (basal, prismatic and pyramidal planes) is likely to promote significant ductility at high temperature. They also concluded that activation of cross-slip must play a key role in the appearance of the brittle-to-plastic transition. Last but not least, grain boundary sliding at high temperatures has also been hypothesized as a possible mechanism for relaxation of internal (incompatibility) stresses [6] but it remains to be proven.

Our current understanding of the high-temperature mechanical behavior of MAX phases comes mostly from work carried out on Ti₃SiC₂, which is the best characterized MAX phase out of more than 80 MAX phases known to date [37]. However, over the last couple of years, Ti₂AlC was identified as one of the most promising MAX phase for high-temperature applications due to the formation of a protective and self-healing α -Al₂O₃ layer both in air and high humidity environments [38-44]. Although some recent studies have shown that mechanical response of Ti₃SiC₂ below and above BPTT can in many aspects be extended (at least qualitatively) to Ti₂AlC [14,15,29], the high-temperature mechanical behavior of Ti₂AlC is far from fully characterized and understood. In this study, the mechanical responses of Ti₂AlC samples with different grain sizes are systematically studied in compression at temperatures ranging from room temperature to 1100 °C. The selected samples are also studied by Electron Backscatter Diffraction (EBSD) to elucidate the evolution of microstructure during loading at different temperatures. In addition, a mathematical model predicting ultimate compressive strength of Ti₂AlC as a function of grain size and test temperature is proposed here.

2. Material and experimental method

Two different Ti₂AlC powder sources were used to prepare samples for this study: Commercial Powders (CP) by MAXthal 211 (Sandvik Heating Technology, Sweden) and in-house Reaction processed Powders (RP). The reaction processed powders were prepared by mixing elemental powders of Ti (99.5%, -325 mesh), Al (99.5%, -325 mesh) and TiC (99.5%, 2 μ m) (all from Alpha Aesar, USA) in molar ratio of Ti: Al:TiC = 1.00:1.05:0.95. Powder mixtures were pressureless sintered in a tube furnace (GSL1600X, MTI Corporation, USA) at 1400 °C under UHP argon and subsequently drill milled and sieved to produce -170 mesh Ti₂AlC powders. The commercial powders were later densified by Spark Plasma Sintering (SPS) also referred to as Electric Current Assisted Sintering (ECAS) at 1300 °C for 15 min under UHP Argon and with an applied pressure of 100 MPa to yield fine-grained samples with high density. The RP were also densified by SPS at 1300 °C, but for longer times, i.e. 45 min, and some of them were additionally heat treated for 8 or 24 h at 1300 °C in a tube furnace under argon atmosphere to produce samples with relatively large grain sizes [14,45]. In addition, one set of samples (denoted as CS) was prepared by cold compaction followed by pressureless sintering of MAXthal 211 at 1500 °C for 4 h in a vacuum of 10⁻² torr. Processing details and nomenclature of all sets of samples are summarized in Table 1.

The density of the sintered samples was measured by the alcohol immersion method, utilizing 200 proof ethanol, based on Archimedes' principle using procedure outlined in [46,47], **Table 1**. X-ray diffraction (XRD) spectra were collected with a diffractometer (D8 Discover, Bruker, USA) to complement phase identification and quantification. The XRD spectra were acquired with Cu-K α radiation at 40 kV and 40 mA in 8° to 80° 2 θ range with a 0.024° step and a rate of 3.5°/min. Microstructural characterization of polished and chemically etched specimens was carried out using field emission scanning electron microscopy (Quanta 600 FEG, FEI, USA) equipped with Back-Scattered Electron (BSE) detector and Energy-Dispersive Spectroscopy (EDS) system (Oxford Instruments, UK). The grain sizes and the volume percent of intermetallic impurities in samples processed using different procedures were determined from their BSE images using Image J software and reported in **Table 1**.

Room and high temperature uniaxial quasi-static compression tests were performed on cylindrical specimens 5 mm diameter by 8 mm length, machined by Electron Discharge Machining (EDM). The cylindrical specimens were tested in a servo-hydraulic testing machine (MTS-810, MTS, USA) equipped with a vertical split furnace and SiC pushrods. The tests were conducted at a fixed crosshead displacement rate giving a nominal strain rate of $10^{-4}s^{-1}$. A high-temperature axial extensometer (632.59E-77, MTS, USA) was attached to SiC spacers while the specimen's temperature was monitored with a

Table 1
Summary of processing conditions, amount and type of impurities and grain sizes of all samples tested in this study. *Note*: CS refers to Cold Compaction, CP refers to Commercial Powder, RP refers to Reaction Processed, PS refers to Pressure-less Sintering, SPS refers to Spark Plasma Sintering, CG, MG and FG refers to Coarse, Medium and Fine Grain, respectively, and AR is the aspect ratio.

Sample	Powder Source	Sintering Technique	Post Heat Treatment	Density	Secondary Phases Detected			Grain Size		
								Length	Thickness	AR
			(hr.)	g/cm ³	XRD	SEM/EDS	Vol% TiAl _x	(μm)	(µm)	
CS-CG	Maxthal 211	PS 1500 °C 4 hr.	0	3.98	TiAl _x ; Ti ₃ AlC ₂ ; Ti ₅ Al ₂ C ₃	TiAl _x ; Ti ₃ AlC ₂ ; Ti ₅ Al ₂ C ₃ ; Al ₂ O ₃	17	22 ± 22	5 ± 2.6	4.4
CP- FG	Maxthal 211	SPS 1300 °C 15 min.	0	4.03	TiAl _x ; Ti ₃ AlC ₂	TiAl _x ; Ti ₃ AlC ₂ ; Al ₂ O ₃	7	4.2 ± 2.5	2.1 ± 1	2.1
RP-FG	RP	SPS 1300 °C 45 min.	0	4.02	_	TiAl _x ; Al ₂ O ₃	3	6.1 ± 2.8	4.6 ± 2.2	1.4
RP-MG	RP	SPS 1300 °C 45 min.	8	4.02	_	TiAl _x ; Al ₂ O ₃	3	13.9 ± 8	7.3 ± 2.4	1.9
RP-CG	RP	SPS 1300 °C 45 min.	24	4.02	_	TiAl _x ; Al ₂ O ₃	3	17.4 ± 9.7	$\textbf{8.2} \pm \textbf{2.9}$	2.2

K-type thermocouple that was placed in direct contact with the spacers. Heating rates were limited to less than 600 °C per hour and a soaking time of 15 min was used to allow the sample to equilibrate to testing temperature.

In addition, the microstructures of two sample sets, RP-FG and RP-CG in the as-sintered condition and after loading in compression at 20 °C, 700 °C, and 1100 °C, were examined by Electron Backscatter Diffraction (EBSD). The metallographic specimens of these samples were mechanically polished down to 0.1 μ m and then polished using colloidal silica so as to provide a smooth finish and secured in pre-tilted 70° specimen holder to provide the high tilt angle required for EBSD. The EBSD process was performed using Field Emission Gun Scanning Electron Microscope (Zeiss Ultra Plus, Carl Zeiss, Oberkochen, Germany) operating with an accelerating voltage of 20 kV. An area of 250 μ m by 250 μ m was scanned in each specimen with a step size of 0.2 μ m. Data acquisition and analysis were performed using Oxford Instrument's AZTecHKL and HKL Tango and Mambo software.

3. Experimental results and discussion

3.1. Initial microstructure of as-processed samples

The Back-Scattered Electron (BSE) images of five as-processed Ti₂AlC specimens, namely CP-FG (Commercial Powder — Fine-Grained), RP-FG (Reaction processed Powder — Fine-Grained), RP-MG (Reaction processed Powder — Medium-Grained), RP-CG

(Reaction processed Powder - Coarse-Grained), and CS-CG (Commercial powder cold compacted followed by pressureless Sintering - Coarse-Grained) are shown in Fig. 1. Several BSE images like those shown in Fig. 1 of the samples were used to measure length, thickness and aspect ratio of over 100 grains in each sample. The results of the grain size measurements are summarized in Table 1. As listed in Table 1, the average grain lengths and thicknesses varied from 4.2 ± 2.5 to $22 \pm 22~\mu m$ and from 2.1 ± 1 to $8.2 \pm 2.9~\mu m$, respectively, in samples fabricated via different processing routes. Note that the BSE image of the specimen of CS-CG sample shown in Fig. 1e is unetched. Similar BSE images of mechanically polished but unetched specimens were used together with EDS analysis to determine the volume fraction of TiAl_x as $Vol_{TiAl}\% = {Area_{TiAl} \choose Area_{Total}}*100\%$ in all the microstructures and the results are summarized in Table 1. In all the samples, TiAlx was determined to be the major impurity phase that can be easily distinguished from Ti₂AlC as a dark gray phase in BSE images, see Fig. 1e. The results of XRD analyses (not shown here) are also summarized in Table 1 and show that all samples prepared from RP were pure, while those prepared from commercial powders contained not only TiAlx, but also Ti₃AlC₂ and Ti₅Al₂C₃. Additional phase composition studies of samples processed from RP using EBSD (not shown here) also confirmed their high purity since less than 3.3% of Al₂O₃, 1.4% of TiAl_x, and 0.16% of TiC were detected in all examined samples, which is a slightly higher amount of impurities than that determined from SEM/EDS results in Table 1.

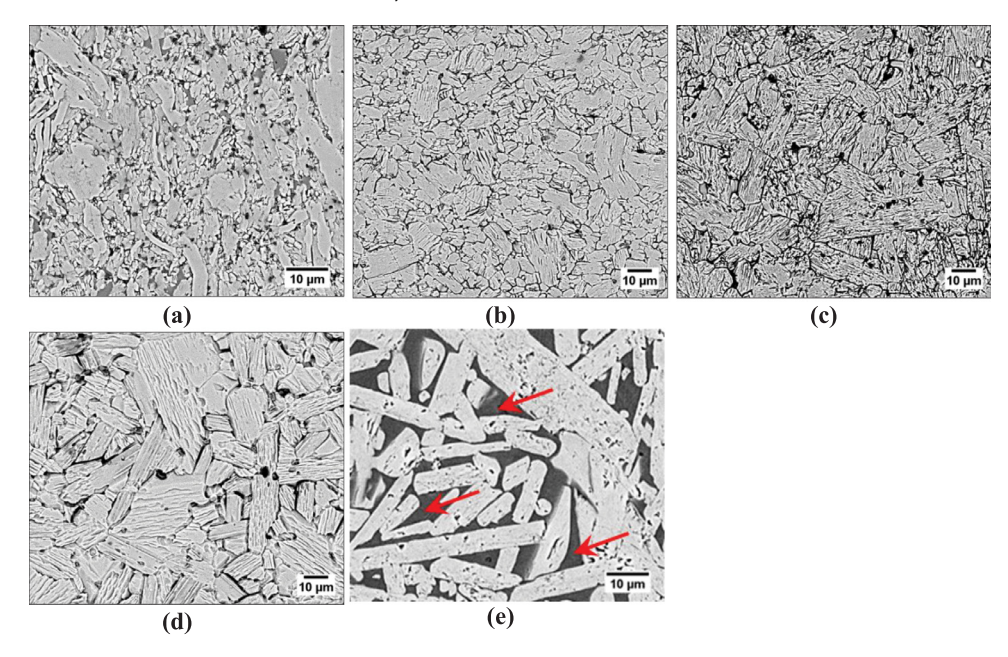
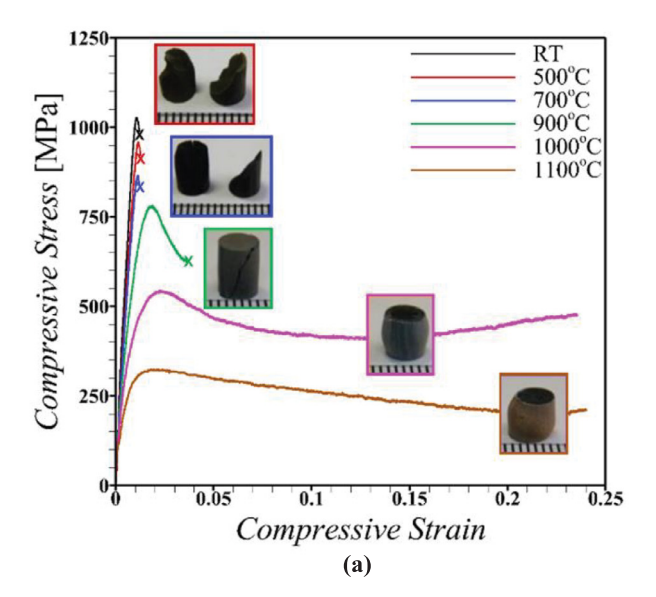


Fig. 1. Typical Back-Scattered Electron (BSE) micrographs of specimens of: (a) etched CP-FG; (b) etched RP-FG; (c) etched RP-MG; (d) etched RP-CG; and (e) unetched CS-CG. In (e) the dark gray phase between Ti₂AlC grains denoted by arrows were identified by EDS as TiAl_x.

3.2. Mechanical response under thermomechanical loading

Selected but typical compressive stress-strain response of RP-FG and RP-CG Ti₂AlC samples at six different test temperatures ranging from room temperature (RT) to 1100 °C are shown in Fig. 2a and b. respectively. The compressive stress-strain response shown in Fig. 2, is qualitatively in-line with the previously reported stress-strain response for Ti₂AlC and other MAX phases under compression [7, 48-51]. As shown in Fig. 2, below a certain test temperature, both the fine- and the coarse- grained specimens subject to monotonically increasing compressive deformation, initially exhibit elastic stress-strain response which is soon followed by brittle fracture with an insignificant inelastic deformation. But for test temperatures greater than 700 °C, both the fine- and the coarse-grained specimens undergo brittle to plastic transition, with the amount of inelastic deformation increasing with increasing temperature. Both the fine- and the coarse-grained specimens tested at 900 °C underwent more graceful failure as it is indicated with the larger "tail" or softening between maximum and failure



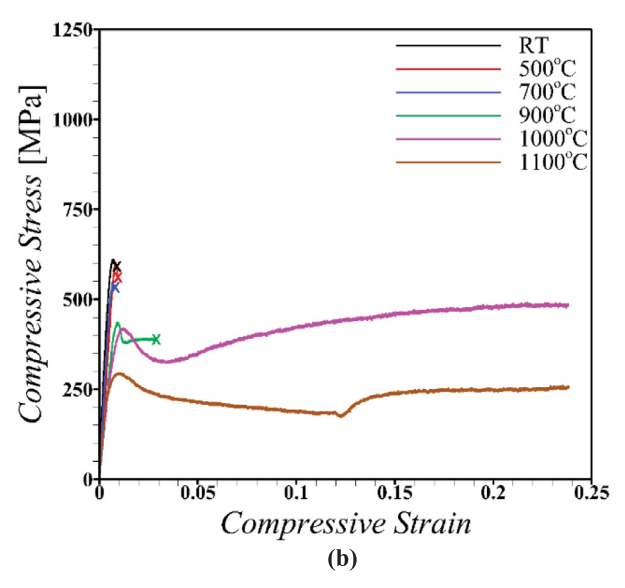


Fig. 2. Typical stress-strain curves obtained from compressive testing of **(a)** RP-FG and **(b)** RP-CG samples at different temperatures. *Note*: The specimens tested at 1000 °C and 1100 °C were interrupted before final failure. Inserts show specimens after completion of testing.

stresses. For test temperatures greater than 900 °C, neither fine- nor coarse-grained specimens underwent failure under compression at least until a compressive strain of \approx 24%, after which the tests were discontinued since the upper limit of the extensometer was reached. The specimens tested at temperatures above the brittle to plastic transition temperature (BPTT) underwent significant softening after reaching the maximum stress level. At least for the specimens tested at 1000 °C, the extensive softening is followed by apparent hardening at higher strain levels as shown in Fig. 2. The apparent hardening in the compressive stress-strain response of these specimens is likely due to the extensive lateral expansion or barreling of the specimens.

To further analyze the brittle-to-plastic transition, the average strain to failure of all specimens tested in this study are plotted as a function of test temperature, **Fig. 3**. As shown in the figure, none of the specimens tested above 900 °C underwent failure under compression at least until 0.23 compressive strain. The strain to failure of the specimens of all five samples tested at 700 °C or below approximately lies in the range of 0.01 to 0.02. The strain to failure of the specimens of the CP-FG, RP-FG, RP-MG, and RP-CG samples increased rapidly for test temperatures 900 °C and above. This suggests that the BPTT for these samples lies somewhere in between 700 °C and 900 °C. This range is similar to previously reported range of 800 °C – 900 °C for Ti₂AlC MAX phases processed via a different route [52].

The effects of the test temperature and microstructural parameter such as grain length on compressive strength of Ti₂AlC MAX phases are shown in Fig. 4. The compressive strength of all five samples as a function of the test temperature is shown in Fig. 4a, while the dependence of compressive strength on the initial grain length for all six test temperatures ranging from room temperature (RT) to 1100 °C is shown in Fig. 4b. As shown in Fig. 4a and previously reported for Ti₃SiC₂ MAX phases [7, 33], the compressive strength of all five samples of Ti₂AlC MAX phase strongly depends on grain length below BPTT, with greater compressive strength for fine-grained samples. However, with increasing test temperature the compressive strength of the specimens of fine-grained samples decreases more rapidly, and above BPTT the difference between the compressive strengths of the samples with different grain length seems to vanish. The dependence of compressive strength on initial grain length for a fixed test temperature can be seen more clearly in Fig. 4b, where the compressive strength is plotted as function of $1/\sqrt{l}$, where l is the initial grain length. As shown in Fig. 4b, below 900 °C or BPTT, all samples show

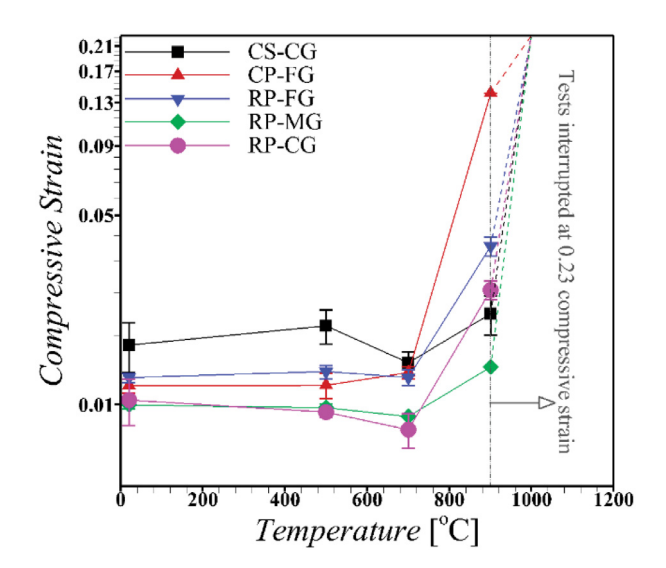
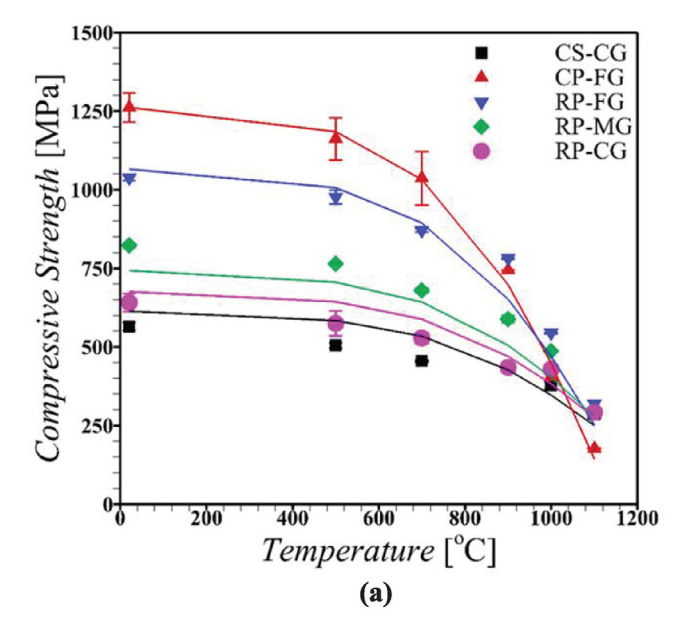


Fig. 3. Average compressive strain as a function of temperature. The maximum strain recorded at and above $1000~^{\circ}\text{C}$ is 0.23 for all specimens since the tests were interrupted before failure.



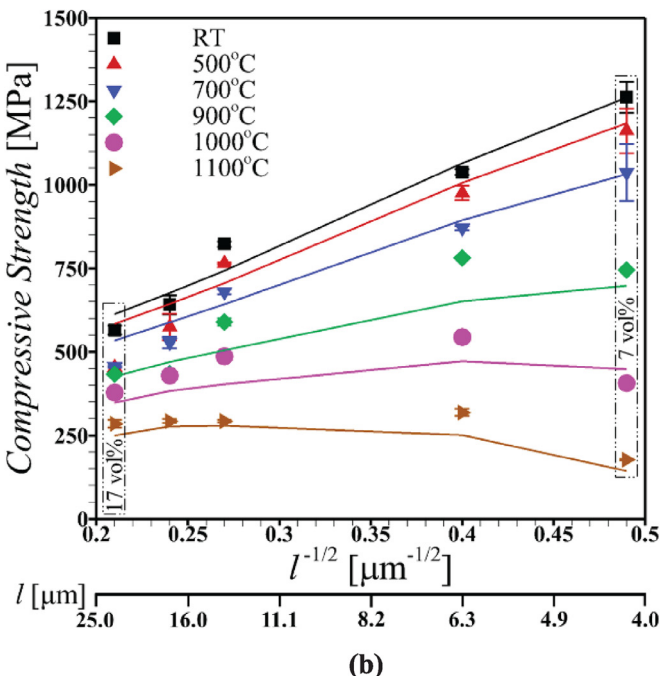


Fig. 4. (a) The variation of compressive strength as function of test temperature for all five samples. (b) Compressive strength plotted in the Hall-Petch manner as a function of $1/\sqrt{l}$, where l is the average grain length. In both (a) and (b), the symbols are the experimentally measured values with error bars, while the solid lines are modeling predictions. The volume fraction of TiAl_x for two samples with average grain length $22~\mu m$ and $4.2~\mu m$ are marked in (b).

an Hall-Petch type relationship between compressive strength and grain length, i.e. roughly a linear dependence of compressive strength on $1/\sqrt{l}$. The Hall-Patch type relationship between compressive strength and grain length at low test temperatures has been previously associated with the dislocation pile up at grain boundaries between soft and hard grains that in turn leads to high stress concentrations and formation of Zener-Stroh type cracks or Mode II fracture [14]. But for test temperatures of 900 °C or above the dependence of compressive strength on $1/\sqrt{l}$ decreases, and for test temperature as high as 1100 °C the dependence of compressive strength on $1/\sqrt{l}$ exhibit an inverse Hall-Petch effect (strength decreases with decreasing grain length, l). As also shown in Fig. 4b, the amount of TiAl_x impurities in the microstructure does not significantly affect the

aforementioned dependence of compressive strength on grain length for the range of test temperatures considered in this work. For instance, neither the behavior of the samples with the highest amount of $TiAl_x$ i.e. 17 vol% nor with the lowest amount of $TiAl_x$ i.e. 7 vol% deviate from the observed trends.

3.3. Microstructural changes post thermomechanical loading

As discussed under Section 3.2, with increasing test temperature the compressive strength of the specimens of fine-grained samples decrease more rapidly, and above BPTT the difference between the compressive strengths of the samples with different grain length seems to vanish. In order to better understand the effect of the test temperature on the mechanical response of Ti₂AlC MAX phases under compression, we characterized the changes in microstructure of the specimens of RP-FG (fine-grained) and RP-CG (coarse-grained) samples post deformation at two temperatures: 700 °C (below the BPTT) and 1100 °C (above the BPTT). Note that at 1100 °C the compressive strength of RP-FG and RP-CG are roughly the same, Fig. 4a.

The results of extensive EBSD analyses of the specimens of RP-FG and RP-CG samples deformed under compression at 700 °C and 1100 °C are summarized in Fig. 5 for RR-FG and in Fig. 6 for RP-CG samples. For comparison, some of the previously reported EBSD results of specimens of both RP-FG and RP-CG samples in the as-processed and loaded to 500 MPa at room temperature (labeled 20 °C) conditions are also shown in Figs. 5 and 6 [15]. Results in those figures are organized in four columns where:

- IPF column shows inverse pole figures;
- GBs column shows low angle grain boundaries (LAGB) with misorientation angles across boundary ranging from 2° to 10° as red lines, together with high angle grain boundaries (HAGB) defined by misorientation exceeding 10° as black lines;
- BC+UI shows band contrast and unindexed area indicating quality of the EBSD results and damage (pores, microcracks, etc.) accumulation in the microstructure;
- SF+GB shows Schmid factor maps for (0001)[1120] slip system together with LAGB as red lines and HAGB as black lines.

A comparison of the results presented in **Figs. 5** and **6** shows that the amount of LAGBs, denoted by red lines in GBs columns, increases with increasing test temperatures in both the fine- and coarse-grained microstructures. The SF+GBs columns in **Figs. 5** and **6** confirm that these LAGBs preferentially form in the grains with high Schmid factors. A comparison of the results in BC+UI columns in **Figs. 5** and **6** shows that the fraction of unindexed area also increases with increasing test temperature. The UI area is a good indication of damage accumulation in the form of intergranular cracks, delamination and highly localized deformation in the region analyzed via EBSD. The increase in damage accumulation in Ti₂AlC MAX phases with increasing test temperature, is in-line with past observations of significant amount of damage accumulation during high temperature (creep) deformation of other MAX phases such as Ti₃SiC₂ [7,30–32].

In order to further highlight the differences and similarities in the final microstructures of specimens of RP-FG and RP-CG samples deformed under compression at 1100 °C, two selected areas from EBSD analyses of these specimens are shown in Figs. 7 and 8, respectively. We first discuss the similarities. At 1100 °C, both RP-FG and RP-CG samples have roughly the same compressive strength (Fig. 4a) and show formation of LAGBs preferentially in the grains with high Schmid factors (Figs. 7 and 8). These LAGBs have the configurations of close and open loops, or straight lines that span from one grain boundary to another. The formation of these LAGBs are likely due to kinking, delamination and/or formation of DWs, following the observation of microstructural evolution in Ti₃SiC₂ during high temperature creep [53]. Next, we focus on the differences. A qualitative comparison of

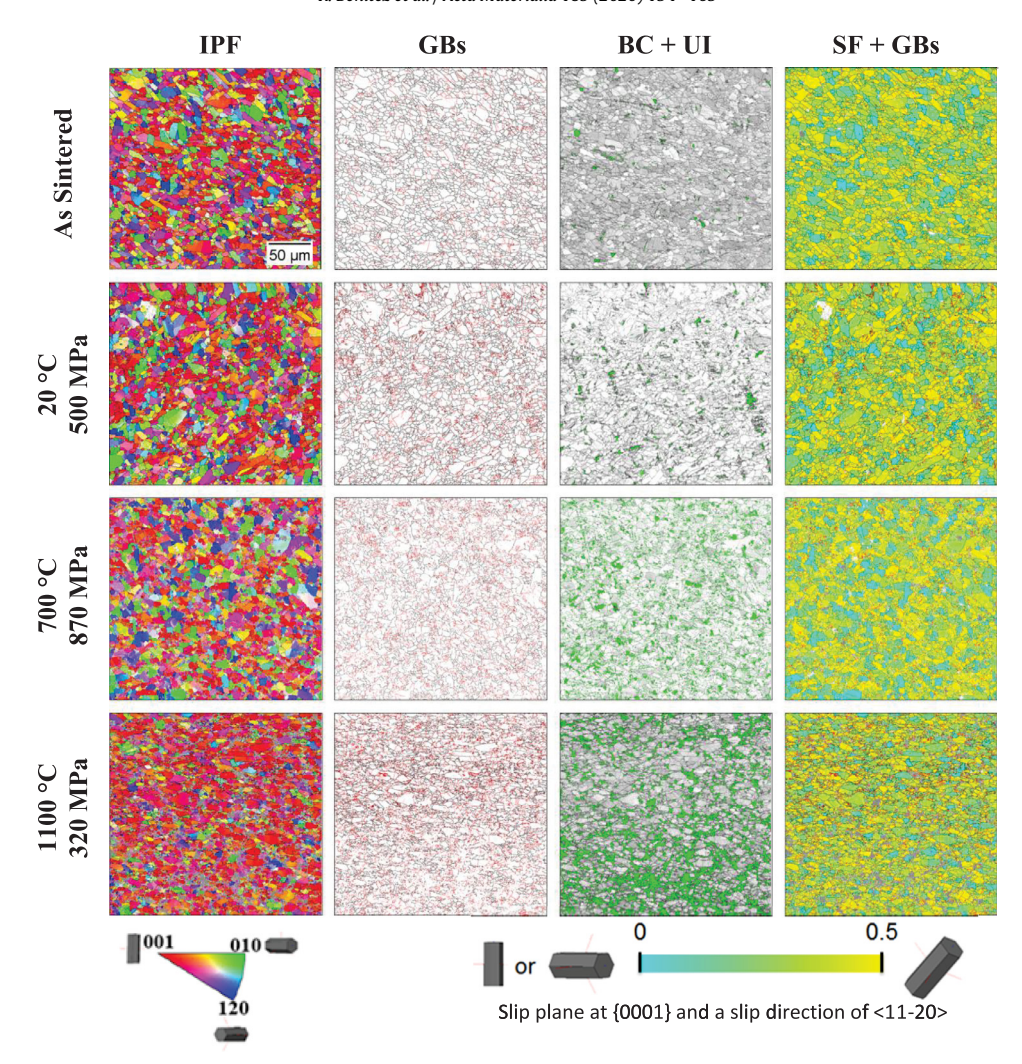


Fig. 5. EBSD maps for RP-FG specimens. Columns from left to right are labeled: (IPF) for Inverse pole figures; (GBs) for grain boundaries with black indicating high angle grain boundaries where misorientation exceeds 10° and with red for low angle grain boundaries for those between 2° and 10°; (BC + UI) for band contrast and unindexed area in green; (SF + GBs) for Schmid factors with blue indicating zero and yellow indicating the maximum of 0.5 and with grain boundaries showing with the before mentioned criteria. The rows indicate test conditions and from top to bottom are for: as-sintered specimen; specimen loaded to 500 MPa at 20 °C; specimen loaded to failure at 700 °C that exhibited 870 MPa peak stress; and for specimen deformed at 1100 °C and exhibited peak stress of 320 MPa but no macroscopic failure. (For interpretation of the references to colour in this figure legend, the reader is referred to the web version of this article.)

Figs. 7 and 8 shows that the amount of LAGBs is greater in the coarse-grained microstructure (RP-CG) than the fine-grained microstructure (RP-FG). The increased amount of LAGBs in the coarse-grained microstructure is likely due to the fact that in MAX phases, crystallographic slip is predominantly limited to basal planes that results in larger incompatibility stresses in coarse-grained microstructures [14]. These stresses are in turn relieved by the formation of kink-bands (KBs). The formation of KBs in MAX phases only results in moderate softening or a drop in strength because KBs effectively stop delamination cracks [6]. Now, assuming that the crystallographic slip becomes easier with increasing test temperature, it is then intuitive that the formation of LAGBs in coarse-grained microstructures will increase with increasing test temperatures without significant softening.

We also quantified the number of grains in a 250 μ m -by-250 μ m area in the as-sintered, loaded to 500 MPa at room temperature (labeled as 20 °C), deformed at 700 °C and at 1100 °C specimens of both the fine-grained (RP-FG) and coarse-grained (RP-CG) samples. The results are presented in **Fig. 9**. As shown in the figure, the number of grains does not change in the fine-grained microstructure during compressive deformation below BPTT. But above BPTT the number of grains in the microstructure increases. In coarse-grained microstructure, there is an increase in the number of grains even at

test temperatures below BPTT, and above BPTT, the number of grains in the microstructure increases drastically.

Next, we characterized the texture evolution in fine-grained (RP-FG) and coarse-grained (RP-CG) microstructures post thermomechanical loading. The contoured pole figures of the specimens of RP-FG and RP-CG samples deformed under compression at 700 °C and 1100 °C together with the as-processed and loaded to 500 MPa at room temperature conditions are shown in Fig. 10. From Fig. 10, it can be clearly seen that no significant texture development occurs in the specimens of the fine-grained samples below BPIT. However, above BPIT the specimens of fine-grained samples are highly textured with more grains oriented for easy slip. This observation correlates well with the significant softening in fine-grained microstructures above BPTT, Fig. 4a. on the other hand, there is no significant development of texture in the specimens of coarse-grained samples.

4. Modeling the influence of microstructure and temperature on compressive strength

We now focus on quantifying the effect of the initial microstructure i.e. grain length and test temperature on the compressive strength of Ti₂AlC MAX phases. As discussed under Section 3.2, the

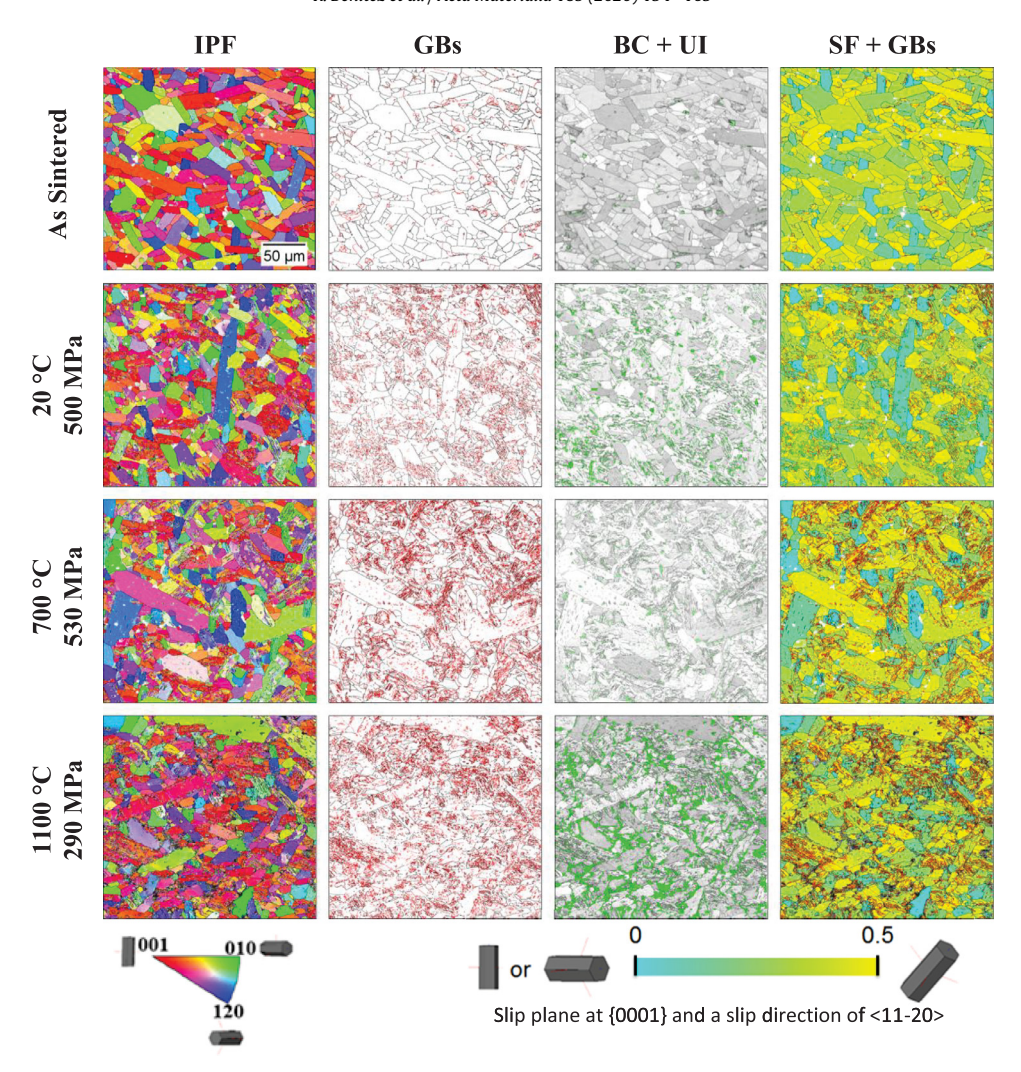


Fig. 6. EBSD maps for RP-CG sample. Columns from left to right are labeled: (IPF) for Inverse pole figures; (GBs) for grain boundaries with black indicating high angle grain boundaries where misorientation exceeds 10° and with red for low angle grain boundaries for those between 2° and 10°; (BC + UI) for band contrast and unindexed area in green; (SF + GBs) for Schmid factors with blue indicating zero and yellow indicating the maximum of 0.5 and with grain boundaries showing with the before mentioned criteria. The rows indicate test conditions and from top to bottom are for: as-sintered specimen; specimen loaded to 500 MPa at 20 °C; specimen loaded to failure at 700 °C that exhibited 530 MPa peak stress; and for specimen deformed at 1100 °C and exhibited peak stress of 290 MPa but no macroscopic failure. (For interpretation of the references to colour in this figure legend, the reader is referred to the web version of this article.)

compressive strength of all five samples of ${\rm Ti_2AlC}$ MAX phases strongly depends on grain length below BPTT, with greater compressive strength for fine-grained samples, in-line with the Hall-Petch strengthening mechanism in a polycrystalline material. But with increasing test temperature the compressive strength of the specimens of fine-grained structure decrease more rapidly, and above BPTT the difference between the compressive strengths of the samples with different grain length seems to vanish. Additionally, at even higher temperatures the compressive strength of ${\rm Ti_2AlC}$ MAX phases exhibits an inverse Hall-Petch effect i.e. the strength decreases with decreasing grain length, l, or increasing $1/\sqrt{l}$, as shown in Fig. 4.

For a polycrystalline material, the Hall-Petch strengthening with grain length, l, is given as:

$$\sigma_{HP}(l) = \sigma_0 + k_{HP}l^{-1/2} \tag{1}$$

where, σ_0 and k_{HP} , are material dependent Hall-Petch parameters. The classical Hall-Petch strengthening relation, Eq. (1), for a polycrystalline material is temperature (T) independent. The temperature dependence can be introduced to the Hall-Petch relation via the temperature dependence of the shear modulus, G, of the material and assuming that the Poisson's ratio of the material is temperature independent [54,55], so that,

$$\sigma_{HP}(l,T) = \sigma_0 + \left[\frac{G(T)}{G_{293K}}\right]^{1/2} k_{HP} l^{-1/2}$$
 (2)

The temperature corrected Hall-Petch relation in Eq. (2) predicts that the effect of grain length on the strength of the material mildly decreases with increasing temperature through the temperature dependence of the shear modulus, G. The Eq. (2) still, however, predicts an increase in strength of a polycrystalline material with decreasing grain length. This is in contrast with the measured grain length dependent compressive strength of the Ti_2AlC MAX phases as a function of the test temperature shown in Fig. 4b.

As discussed under Section 3.3, the initially coarse-grained microstructure undergoes significant grain refinement with increasing test temperature compared to initially fine-grained microstructure, Fig. 9. However, the compressive strength of initially fine-grained microstructure decreases more rapidly with increasing test temperature as compared to initially coarse-grained microstructure, Fig. 4a. This suggests that the grain refinement is not the primary factor contributing to thermal induced softening. Also, the stress-strain curves obtained under compression for both the initially fine- and coarse-grained microstructures, Fig. 2, do not corroborate with any

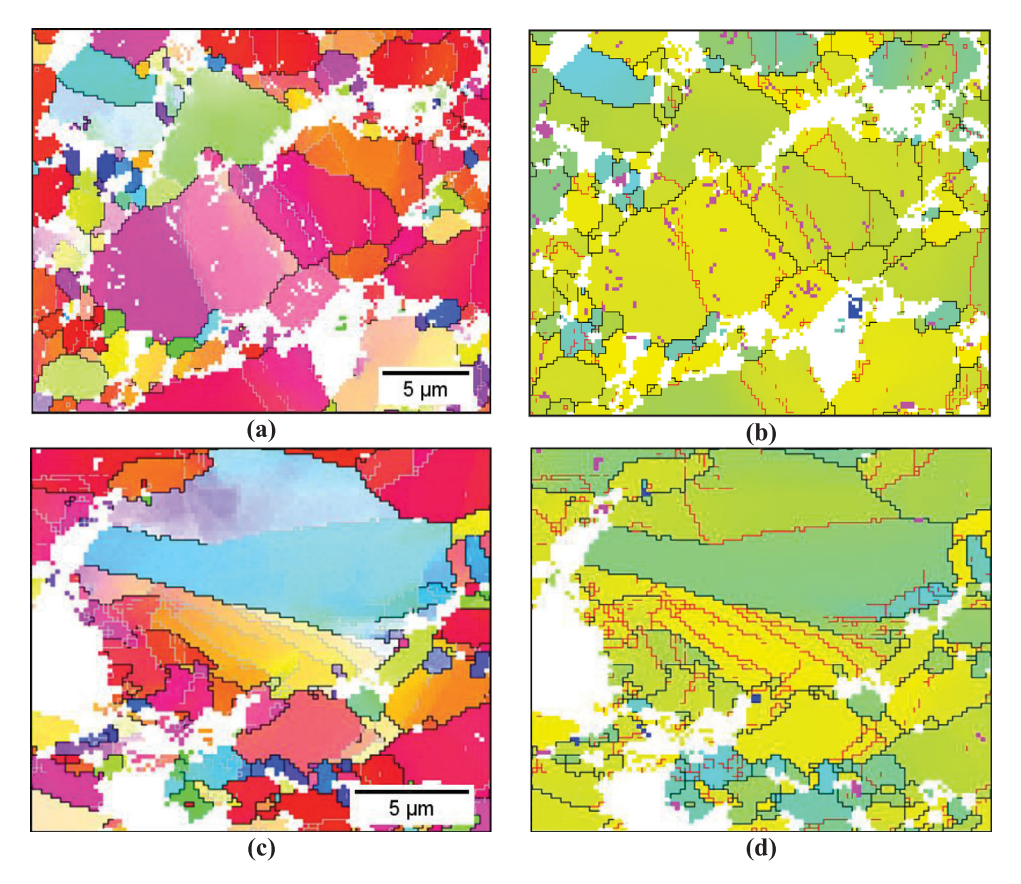


Fig. 7. (a & c) Two selected areas from EBSD maps for RP-FG after testing in compression at 1100 °C showing inverse pole figures (IPF). (b & d) Schmid factors (SF) and grain boundaries (GBs) as in Figs. 5 and 6, and alumina (Al₂O₃) as a major indexed imurtity in magenta in the same regions shown in a and c, respectively. Note that low Schmid factor grains, aqua and green have little or no LAGBs within, while the high Schmid factor grains have large number of LAGBs with some transitioning to HAGBs resulting in grain refinement (For interpretation of the references to colour in this figure legend, the reader is referred to the web version of this article.).

hardening due to grain refinement during the compressive deformation. But as shown in Fig. 10, post deformation above BPTT, the specimens of fine-grained samples are highly textured with more grains oriented for easy slip. This suggests activation of grain boundary sliding at high temperatures, that is more pronounced in fine-grained samples than in coarse-gained ones. Thus, we hypothesize that the breakdown of the Hall-Petch effect or the inverse Hall-Petch effect shown in Fig. 4b, is due to the activation of high temperature creep deformation in Ti_2AlC MAX phases. Previous works on various MAX phases have indeed shown that at sufficiently high temperatures, MAX phases can undergo thermally activated creep deformation [29–32].

The steady-state creep strain rate as a function of stress, overall grain size (d) and temperature can in general be given as [56–58],

$$\dot{\varepsilon}(\sigma,\ d,\ T) \propto \left(\frac{1}{d}\right)^p \sigma^n \exp\left(\frac{-Q}{RT}\right) \eqno(3)$$

In Eq. (3), p is the grain size exponent, n is the stress exponent, Q is the activation energy and R is the ideal gas constant. For a constant strain rate loading condition, Eq. (3) can be rewritten as,

$$\sigma(d,T) \propto d^{p/n} \exp\left(\frac{Q}{nRT}\right) \tag{4}$$

We now consider the dependence of σ , on d and T in Eq. (4) as an additional weakening factor, F_w , causing the strength of the material to drop below the predicted Hall-Petch strength. Following this the grain size and temperature dependent strength can be given as,

$$\sigma(d,T) = \left(1 - \frac{1}{F_w}\right)\sigma_{HP} \tag{5}$$

with

$$F_w = k_T d^{p/n} \exp\left(\frac{Q}{nRT}\right) \tag{6}$$

and σ_{HP} is given by Eq. (2). In Eq. (6), k_T is the proportionality constant from Eq. (4).

From the experimental data of Radovic et al. [28], the dependence of shear modulus, *G*, of Ti₂AlC on test temperature can be given as,

$$G(T) = G_{293K} - k_G(T - 293) \tag{7}$$

here, G_{293K} , is the shear modulus of Ti₂AlC at room temperature and k_G is the fitting constant. Now combining Eqs. (2), (5)–(7) gives,

$$\sigma(d, l, T) = \left(1 - \frac{1}{k_T d^{p/n} \exp\left(\frac{Q}{\eta RT}\right)}\right) \left(\sigma_0 + \left[1 - k_G(T - 293)/G_{293K}\right] k_{HP} l^{-1/2}\right)$$
(8)

Note, in Eq. (8) we have two grain size parameters, d and l. This is because the grain morphology of MAX phases is in general not equiaxed. Hence both the length, l, and the thickness, t, of the grains are characterized (see **Table 1**) and a mean grain size is defined as the geometric mean value of the grain lengths and thicknesses, i.e. $d = \sqrt[3]{l^2t}$ as in Tallman et al. [29]. Previous works [14] on MAX phases have correlated the Hall-Petch type dependence of strength with the grain length, l, as also shown in **Fig. 4b**. But we hypothesize that the additional thermal induced creep weakening effects must be correlated with the overall grain size, d.

The final Eq. (8) contains eight parameters, k_T , p, n, Q, σ_0 , k_G , G_{293K} and k_{HP} that needs to be determined. The values of parameters, $k_G = 17.89 \text{MPa} \cdot \text{K}^{-1}$ and $G_{293K} = 118 \text{GPa}$ are directly obtained from

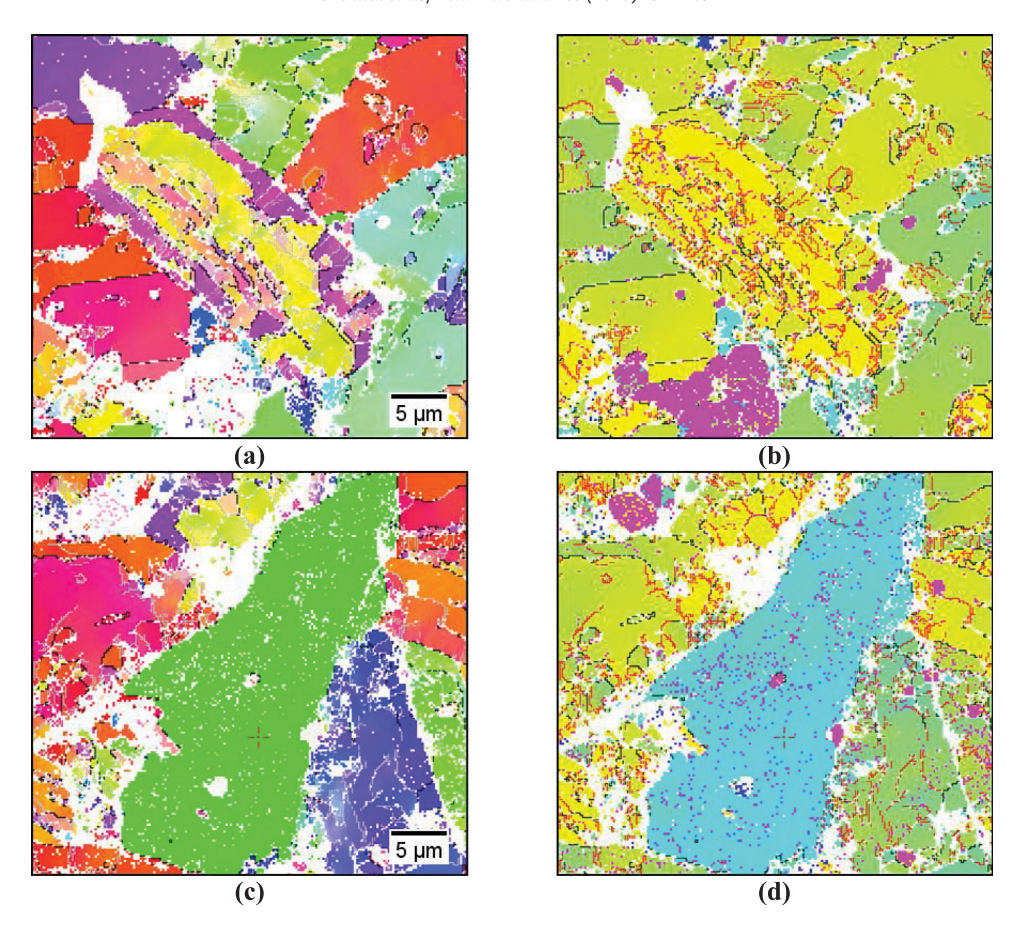


Fig. 8. (a & c) Two selected areas from EBSD maps for RP-CG after testing in compression at 1100 °C showing inverse pole figures (IPF). (b & d) Schmid factors (SF) and grain boundaries (GBs) as in Figs. 5 and 6, and alumina (Al₂O₃) as a major imurity in magenta in the same regions shown in a and c, respectively. Note that grain refinement occurs within the grain with high Schmid factors while grains with low Schmid factors appear free of LAGBs.

the experimental measurements of shear modulus as a function of temperature [28]. The Hall-Petch parameters, $\sigma_0 = 110.6$ MPa and $k_{HP} = 2358$ MPa $\sqrt{\mu m}$, are obtained by fitting Eq. (1) to the experimentally measured compressive strength versus grain length data at room temperature i.e. T = 293 K. The creep stress exponent, n = 2.5, is taken from the experimental measurements of Tallman et al. [29].

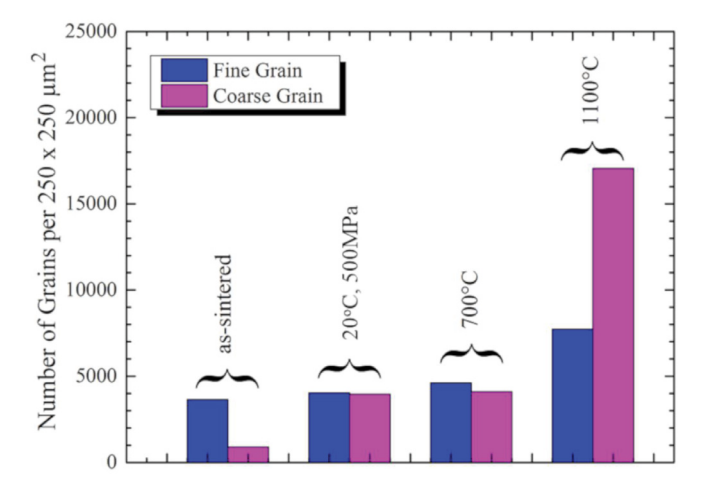


Fig. 9. The number of grains per 250 μ m -by- 250 μ m area scanned are computed by EBSD for fine-grained microstructure (RP-FG) in blue and coarse-grained microstructure (RP-GG) in magenta for (left to right), as-sintered specimens; specimens loaded to 500 MPa at 20 °C; specimens loaded to failure at 700 °C; and for specimens loaded at 1100 °C. (For interpretation of the references to colour in this figure legend, the reader is referred to the web version of this article.)

This reduces the number of parameters in Eq. (8) to three, that are, k_T , p and Q associated with the weakening factor, F_w , in Eq. (6). The values of the parameters $k_T = 0.0089 \mu m^{-p/n}$, p = 0.8 and $Q = 127.5 \text{kJ} \cdot \text{mol}^{-1}$ are obtained from the $\sigma(d, l, T)/\sigma_{HP}(l, T)$ versus temperature data. The value of ideal gas constant is taken to be R = 8.314 J·mol⁻¹·K⁻¹. Note that the activation energy, $Q = 127.5 \text{kJ} \cdot \text{mol}^{-1}$, is roughly a third of the activation energy extracted from the creep tests of Ti₂AlC in Tallman et al. [29]. The low activation energy for thermally activated processes in this work can be due to the fact that in creep tests the imposed nominal stress is held fixed whereas in the high temperature compression experiments the imposed nominal strain rate is held fixed and the internal stress level in the material increases continuously. Also, we note that the activation energy extracted from the creep tests of other MAX phases (e.g. Ti₃SiC₂ [32]) have been reported to depend on the grain size such that the activation energy decreases with decreasing grain size.

The predicted dependence of compressive strength on initial microstructure, characterized by grain size, and test temperature using fully calibrated Eq. (8), together with the experimentally measured data is shown in Fig. 4a and b. As shown in the figure, our proposed model can very well predict the microstructure and temperature dependent compressive strength of the five microstructures of ${\rm Ti}_2{\rm AlC}$ MAX phases at six test temperatures. The model clearly highlights that the thermally induced creep weakening effect is greater in the fine-grained microstructure than in the coarsegrained microstructure. Additionally, it also rationalizes that the thermally induced creep weakening can not only result in the breakdown of the Hall-Petch effect but can also result in an inverse Hall-Petch effect.

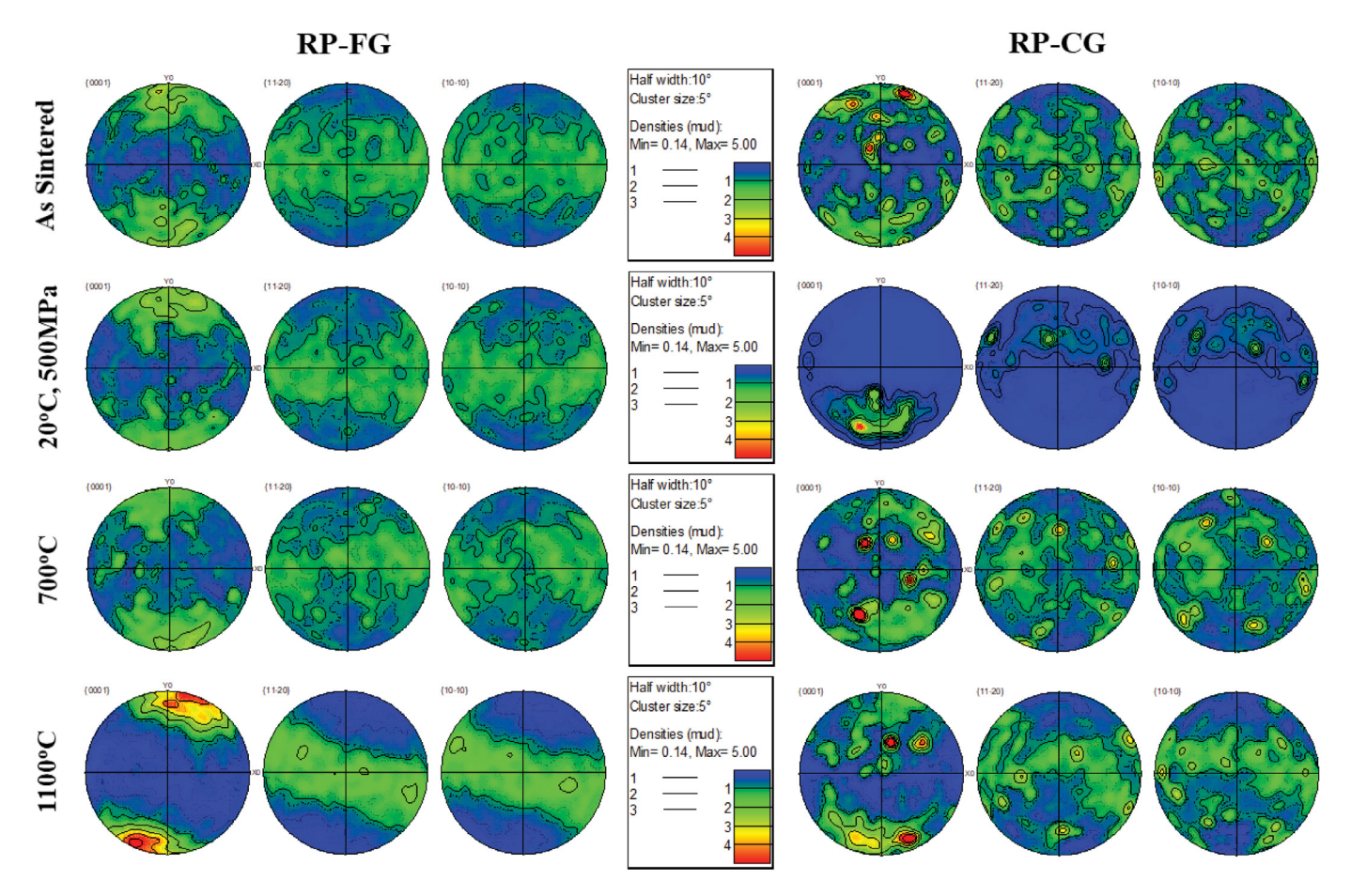


Fig. 10. Contoured pole figures with fixed multiples of uniform density (MUD) value of 5 for RP-FG samples (left) and for RP-CG (right) samples, from top to bottom, in as-sintered condition; loaded to 500 MPa at 20 °C; loaded to failure at 700 °C and loaded at 1100 °C.

Conclusions

High temperature compression test results of Ti₂AlC show that below brittle-to-plastic transition temperature (BPTT) i.e. at around 900 °C, compressive strength increases monotonically with decreasing grain size following a Hall-Petch relationship. However, above BPTT the relationship between compressive strength and grain size is more complex and changes from the Hall-Petch relationship to an inverse Hall-Petch effect. The EBSD results show that the compressive deformation below BPTT results in inhomogeneous deformation and grain refinement in coarse-grained microstructure but not so much in fine-grained microstructure. The compressive deformation above BPTT results in a drastic increase in grain refinement in the coarsegrained microstructure while limited grain refinement is observed in the fine-grained microstructure. The EBSD results also show that the compressive deformation above BPTT results in texture development in fine-grained microstructures with more grains oriented for easy slip, while no significant texture development is observed in coarsegrained microstructures.

A mathematical model has also been formulated to predict the experimentally observed grain size and temperature dependent variation in the compressive strength of Ti₂AlC over a wide range of grain sizes and test temperatures. The model accounts for the competing effects of Hall-Petch strengthening and high temperature creep induced softening mechanisms. The comparison of the model predictions and experimental results clearly show that the model formulated here is in very good quantitative agreement with experimental results. In particular, the model captures very well the gradual decline in compressive strength with increasing test temperature in coarse-grained microstructures as well as the rather rapid decline in

compressive strength with increasing test temperature in finegrained microstructures. To the best of our knowledge, this is the first model developed to predict the variation in strength of MAX phase with different initial microstructures for a wide range of test temperatures

The following can now be concluded about the micromechanisms for the microstructure and temperature dependent strength and stress-induced microstructure evolution of Ti₂AlC. During compressive loading of coarse-grained samples, huge incompatibility stresses develop at relatively low applied stresses as a result of easy basal plane slip in soft grains. Since, kink band (KB) formation is easier in coarse-grained microstructure, these incompatibly stresses are relaxed by kinking. As a result, significant grain refinement occurs in coarse-grained microstructure due to KB accumulation. The delamination associated with KB below BPTT results in lower compressive strengths for coarse-grained microstructures. However, KB effectively stops delamination cracks, so that they do not propagate catastrophically but rather accumulate with increasing load resulting in pseudoductile failure of coarse-grained samples. Both, the basal plane slip and the KB formation becomes easier with increasing temperature, especially above BPTT, resulting in a gradual decrease in compressive strength with increasing test temperature.

On the other hand, in the fine-grained microstructure, the incompatibility stresses that develop due to easy basal plane slip in soft grains during compressive loading is less than in the coarse-grained microstructure. Furthermore, fine-grained microstructure can hardly form KBs since kinking of small grains (with smaller aspect ratio) is difficult. This results in more uniform deformation in fine-grained microstructure and insignificant grain refinement due to lack of KB. The lack of KB in fine-grained microstructures leads to initially high

compressive strength below BPTT. However, at high test temperatures (temperatures close to BPTT), the fine-grained microstructures undergo creep induced grain boundary sliding resulting in texture development with more grains oriented for easy slip. The creep induced softening in fine-grained microstructure at high temperatures exceeds the Hall-Petch strengthening effect thus resulting in significant drop in strength when compared to coarse-grained microstructure.

Note that, even though significant stress-induced grain refinement occurs in coarse-grained microstructures contrary to the behavior observed in fine-grained microstructures due to easier KB formation, no significant texture development is observed in coarse-grained microstructures. This is because the low angle grain boundaries formed due to kinking are quite immobile compared to original high angle grain boundaries. Thus, creep induced grain boundary sliding is difficult in coarse-grained microstructures compared to fine-grained microstructures. A more systematic study on the effect of grain boundary chemistry and structure needs to done to further understand the brittle-to-plastic transition in MAX phases in general.

Declaration of Competing Interest

None

Acknowledgments

This work was supported by National Science Foundation Division of Materials Research (NSF-DMR) under grant 1410983 and Division of Civil, Mechanical, and Manufacturing Innovation (NSF-CMMI) under grant 1729350. In addition, the authors are also grateful for the support of the International Program Development Fund and DVC research/International Research Collaboration Award at the University of Sydney. The authors acknowledge the facilities, and the scientific and technical assistance of Microscopy Australia at the University of Sydney.

References

- [1] M.W. Barsoum, MAXphases: a new class of solids; thermodynamically stable nanolaminates, Progr. Solid State Chem. 28 (1–4) (2000) 201–281.
- [2] M.W. Barsoum, A progress report on Ti₃SiC₂, Ti₃GeC₂, and the H-phases, M₂BX, J. Mater. Synthes. Process. 5 (3) (1997) 197–216.
- [3] M.W. Barsoum, MAX phases: Properties of Machinable Ternary Carbides and Nitrides, Wiley-VCH Verlag GmbH & Co. KGaA, Weinheim, Germany, 2013.
- [4] M.W. Barsoum, T. El-Raghy, Synthesis and characterization of a remarkable ceramic: Ti₃SiC₂, J. Am. Ceramic Soc. 79 (7) (1996) 1953–1956.
- [5] M. Radovic, M.W. Barsoum, MAX phases: bridging the gap between metals and ceramics, Am. Ceramic Soc. Bull. 92 (3) (2013) 20–27.
- [6] M.W. Barsoum, M. Radovic, Elastic and mechanical properties of the MAX phases, Annu. Rev. Mater Res. (2011) 195–227.
- [7] M. Radovic, M.W. Barsoum, T. El-Raghy, S.M. Wiederhorn, W.E. Luecke, Effect of temperature, strain rate and grain size on the mechanical response of Ti₃SiC₂ in tension, Acta Mater. 50 (6) (2002) 1297–1306.
- [8] M.W. Barsoum, L. Farber, I. Levin, A. Procopio, T. El-Raghy, A. Berner, High-resolution transmission electron microscopy of Ti4AlN3, or Ti3Al2N2 revisited, Journal of the Am. Ceramic Soc. 82 (9) (1999) 2545–2547.
- [9] L. Farber, I. Levin, M.W. Barsoum, High-resolution transmission electron microscopy study of a low-angle boundary in plastically deformed Ti₃SiC₂, Philos. Mag. Lett. 79 (4) (1999) 163–170.
- [10] B.J. Kooi, R.J. Poppen, N.J.M. Carvalho, J.T.M. De Hosson, M.W. Barsoum, Ti3SiC2: a damage tolerant ceramic studied with nano-indentations and transmission electron microscopy, Acta Mater. 51 (10) (2003) 2859–2872.
- [11] A. Guitton, S. Van Petegem, C. Tromas, A. Joulain, H. Van Swygenhoven, L. Thilly, Effect of microstructure anisotropy on the deformation of MAX polycrystals studied by in-situ compression combined with neutron diffraction, Appl. Phys. Lett. 104 (24) (2014).
- [12] N.G. Jones, C. Humphrey, L.D. Connor, O. Wilhelmsson, L. Hultman, H.J. Stone, F. Giuliani, W.J. Clegg, On the relevance of kinking to reversible hysteresis in MAX phases, Acta Mater. 69 (0) (2014) 149–161.
- [13] P. Duvai, M.F. Ashby, I. Anderman, Rate-controlling processes in the creep of polycrystalline ice, J. Phys. Chem. 87 (21) (1983) 4066–4074.
- [14] R. Benitez, H. Gao, M. O'Neal, P. Lovelace, G. Proust, M. Radovic, Effects of microstructure on the mechanical properties of Ti₂AlC in compression, Acta Mater. 143 (2018) 130–140.

- [15] R. Benitez, W.H. Kan, H. Gao, M. O'Neal, G. Proust, M. Radovic, Room temperature stress-strain hysteresis in Ti₂AlC revisited, Acta Mater. 105 (2016) 294–305.
- [16] M.W. Barsoum, D. Brodkin, T. El-Raghy, Layered machinable ceramics for high temperature applications, Scr Mater. 36 (5) (1997) 535–541.
- [17] M.W. Barsoum, L. Farber, T. El-Raghy, Dislocations, kink bands, and room-temperature plasticity of Ti₃SiC₂, Metallurg. Mater. Trans. A Phys. Metall. Mater. Sci. 30 (7) (1999) 1727–1738.
- [18] M.W. Barsoum, T. Zhen, S.R. Kalidindi, M. Radovic, A. Murugaiah, Fully reversible, dislocation-based compressive deformation of Ti₃SiC₂ to 1GPa, Nat. Mater. 2 (2) (2003) 107–111.
- [19] M. Barsoum, G. Tucker, Deformation of layered solids: ripplocations not basal dislocations, Scr. Mater. 139 (2017) 166–172.
- [20] M. Barsoum, X. Zhao, S. Shanazarov, A. Romanchuk, S. Koumlis, S. Pagano, L. Lamberson, G. Tucker, Ripplocations: a universal deformation mechanism in layered solids, Phys. Rev. Mater. 3 (1) (2019) 013602.
- [21] J. Griggs, A.C. Lang, J. Gruber, G. Tucker, M. Taheri, M. Barsoum, Spherical nanoindentation, modeling and transmission electron microscopy evidence for ripplocations in Ti3SiC2, Acta Mater. 131 (2017) 141–155.
- [22] J. Gruber, A.C. Lang, J. Griggs, M.L. Taheri, G.J. Tucker, M.W. Barsoum, Evidence for bulk ripplocations in layered solids, Sci. Rep. 6 (2016) 33451.
- [23] C. Zener, The macro-mechanism of fracture, Fractur. Metals (1948) 3.
- [24] A. Stroh, The formation of cracks as a result of plastic flow, Proc. R. Soc. Lond. Ser. A. Math. Phys. Sci. 223 (1154) (1954) 404–414.
- [25] A. Stroh, The formation of cracks in plastic flow. ii, Proc. R. Soc. Lond. Ser. A Math. Phys. Sci. 232 (1191) (1955) 548–560.
- [26] A.G. Zhou, M.W. Barsoum, Kinking nonlinear elastic deformation of Ti₃AlC₂, Ti₂AlC, Ti₃Al(C_{0.5},N_{0.5}), J. Alloys Compd. 498 (1) (2010) 62–70.
- [27] G.P. Bei, G. Laplanche, V. Gauthier-Brunet, J. Bonneville, S. Dubois, Compressive behavior of Ti₃AlC₂ and Ti₃AlO₈Sn_{0.2}C₂ MAX phases at room temperature, J. Am. Ceramic Soc. 96 (2) (2013) 567–576.
- [28] M. Radovic, M.W. Barsoum, A. Ganguly, T. Zhen, P. Finkel, S.R. Kalidindi, E. Lara-Curzio, On the elastic properties and mechanical damping of Ti₃SiC₂, Ti₃SeC₂, Ti₃Si_{0.5}Al_{0.5}C₂ and Ti₂AlC in the 300-1573K temperature range, Acta Mater. 54 (10) (2006) 2757–2767.
- [29] D.J. Tallman, M. Naguib, B. Anasori, M.W. Barsoum, Tensile creep of Ti 2AlC in air in the temperature range 1000-1150°C, Scr. Mater. 66 (10) (2012) 805–808.
- [30] M.W. Barsoum, M. Radovic, P. Finkel, T. El-Raghy, Ti₃SiC₂ and ICE, Appl. Phys. Lett. 79 (4) (2001) 479–481.
- [31] M. Radovic, M.W. Barsoum, T. El-Raghy, S.M. Wiederhorn, Tensile creep of coarse-grained Ti3SiC2 in the 1000-1200°C temperature range, J. Alloys Compd. 361 (1–2) (2003) 299–312.
- [32] T. Zhen, M.W. Barsoum, S.R. Kalidindi, M. Radovic, Z.M. Sun, T. El-Raghy, Compressive creep of fine and coarse-grained Ti₃SiC₂ in air in the 1100–1300 °c temperature range, Acta Mater 53 (19) (2005) 4963–4973.
- [33] T. Zhen, M.W. Barsoum, S.R. Kalidindi, Effects of temperature, strain rate and grain size on the compressive properties of Ti3SiC2, Acta Mater. 53 (15) (2005) 4163–4171.
- [34] Z.F. Zhang, Z.M. Sun, Shear fracture behavior of Ti3SiC2 induced by compression at temperatures below 1000°C, Mater. Sci. Eng. A 408 (1–2) (2005) 64–71.
- [35] J.F. Li, W. Pan, F. Sato, R. Watanabe, Mechanical properties of polycrystalline Ti₃SiC₂ at ambient and elevated temperatures, Acta Mater. 49 (6) (2001) 937–945.
- [36] A. Guitton, A. Joulain, L. Thilly, C. Tromas, Evidence of dislocation cross-slip in MAX phase deformed at high temperature, Sci. Rep. 4 (2014) 6358.
- [37] M. Sokol, V. Natu, S. Kota, M.W. Barsoum, On the chemical diversity of the MAX phases, Trends Chem. (2019).
- [38] S. Li, G. Song, K. Kwakernaak, S. van der Zwaag, W.G. Sloof, Multiple crack healing of a Ti-AlC ceramic. I. Eur. Ceram. Soc. 32 (8) (2012) 1813–1820.
- [39] H.J. Yang, Y.T. Pei, J.C. Rao, J.T.M. De Hosson, S.B. Li, G.M. Song, High temperature healing of Ti₂AlC: on the origin of inhomogeneous oxide scale, Scr. Mater. 65 (2) (2011) 135–138.
- [40] S. Basu, N. Obando, A. Gowdy, I. Karaman, M. Radovic, Long-term oxidation of Ti_{2A}IC in air and water vapor at 1000-1300°C temperature range, J. Electrochem. Soc. 159 (2) (2012) C90-C96.
- [41] X.H. Wang, Y.C. Zhou, High-temperature oxidation behavior of Ti₂AlC in air, Oxidat, Metals 59 (3–4) (2003) 303–320.
- [42] J.W. Byeon, J. Liu, M. Hopkins, W. Fischer, N. Garimella, K.B. Park, M.P. Brady, M. Radovic, T. El-Raghy, Y.H. Sohn, Microstructure and residual stress of alumina scale formed on Ti₂AlC at high temperature in air, Oxid. Metals 68 (1–2) (2007) 97–111.
- [43] D.J. Tallman, B. Anasori, M.W. Barsoum, A critical review of the oxidation of Ti_2AlC , Ti_3AlC_2 and Cr_2AlC in air, Mater. Res. Lett. 1 (3) (2013) 115–125.
- [44] J.L. Smialek, A. Garg, Microstructure and oxidation of a MAX phase/superalloy hybrid interface, NASA/TM—2014-216679, Cleveland (2014).
- [45] P.N. Parrikar, R. Benitez, H. Gao, M. Radovic, A. Shukla, The effect of grain size on deformation and failure of Ti₂AlC MAX phase under thermo-mechanical loading, Exp. Mech. 57 (5) (2017) 675–685.
- [46] L. Hu, R. Benitez, S. Basu, I. Karaman, M. Radovic, Processing and characterization of porous Ti2AlC with controlled porosity and pore size, Acta Mater. 60 (18) (2012) 6266–6277.
- [47] P. Gudlur, A. Forness, J. Lentz, M. Radovic, A. Muliana, Thermal and mechanical properties of al/al₂o₃ composites at elevated temperatures, Mater. Sci. Eng. A 531 (2012) 18–27.
- [48] M.W. Barsoum, M. Ali, T. El-Raghy, Processing and characterization of Ti₂AlC, Ti₂AlN, and Ti₂AlC_{0.5}N_{0.5}, Metall. Mater. Trans. A Phys. Metall. Mater. Sci. 31 (7) (2000) 1857–1865.
- [49] T. El-Raghy, M.W. Barsoum, A. Zavaliangos, S.R. Kalidindi, Processing and mechanical properties of Ti₃SiC₂: II, effect of grain size and deformation temperature, J. Am. Ceram. Soc. 82 (10) (1999) 2855–2860.

- [50] D.T. Wan, F.L. Meng, Y.C. Zhou, Y.W. Bao, J.X. Chen, Effect of grain size, notch width, and testing temperature on the fracture toughness of Ti₃Si(Al)C₂ and Ti₃AlC₂ using the chevron-notched beam (CNB) method, J. Eur. Ceram. Soc. 28 (3) (2008) 663–669.
- [51] W. Tian, Z. Sun, H. Hashimoto, Y. Du, Compressive deformation behavior of ternary compound Cr2AlC, J. Mater Sci. 44 (1) (2009) 102–107.
- [52] Y. Bai, X. He, R. Wang, Y. Sun, C. Zhu, S. Wang, G. Chen, High temperature physical and mechanical properties of large-scale Ti₂AlC bulk synthesized by self-propagating high temperature combustion synthesis with pseudo hot isostatic pressing, J. Eur. Ceram. Soc. 33 (13–14) (2013) 2435–2445.
- [53] F. Barcelo, S. Doriot, T. Cozzika, M. Le Flem, J.L. Béchade, M. Radovic, M.W. Barsoum, Electron-backscattered diffraction and transmission electron microscopy study of post-creep Ti₃SiC₂, J. Alloys Compd. 488 (1) (2009) 181–189.
- [54] J. Hirth, J. Lothe, Theory of Dislocations, 2nd ed., McGraw-Hill, New York,
- [55] J.H. Schneibel, M. Heilmaier, Hall–Petch breakdown at elevated temperatures, Materials Transactions $55\,(1)\,(2014)\,44-51.$
- [56] J. Bird, A. Mukherjee, J. Dorn, Correlation between high-temperature creep behavior and structure, in: D.G. Brandon, A. Rosen (Eds.), Proceedings of a Symposium on Quantitative Relation Between Properties and Microstructure, University Press, IsraelJerusalem, 1969, pp. 255–342.
- [57] A.K. Mukherjee, J.E. Bird, J.E. Dorn, Experimental correlations for high-temperature creep, Trans. Am. Soc. Metals 62 (1969) 155–179.
- [58] A.K. Mukherjee, The rate controlling mechanism in superplasticity, Mater. Sci. Eng. 8 (2) (1971) 83–89.